nature communications

Article

https://doi.org/10.1038/s41467-025-62019-y

Nanowhisker glues for fatigue-resistant bioadhesion and interfacial functionalization

Received: 24 July 2024

Accepted: 8 July 2025

Published online: 24 July 2025

Check for updates

Shuaibing Jiang[1,7], Tony Jin[2,7], Tianqin Ning[1], Zhen Yang[1], Zhenwei Ma[1], Ran Huo[1], Yixun Cheng[1], Davis Kurdyla[3], Edmond Lam[2,3], Rong Long[4], Audrey Moores[2,5] ✉ & Jianyu Li[1,6] ✉

Fatigue-resistant functional bioadhesion is desired in diverse applications ranging from wound management to wearable devices. Nanoparticle-based bioadhesives offer versatile functionality but suffer from weak adhesion and fatigue vulnerability due to tissue barriers and poor tissue interactions. Polymer chain-based bioadhesives can form tough bioadhesion but remain vulnerable to fatigue fracture. Here we demonstrate that rationally designed chitosan nanowhiskers glues achieve fatigue-resistant bioadhesion and interfacial functionalization via the combined high aspect ratio, rigidity, polymer-binding and network-forming properties. We deploy these glues using chemical enhancers, microneedle rollers, and ultrasound, enabling strong tissue anchorage despite tissue barriers. At low concentrations, the nanowhisker glue paired with a tough hydrogel achieves an interfacial fatigue threshold of 382 J m^{-2} and adhesion energy exceeding 1000 J m^{-2}. Transmission electron microscopy reveals a sandwiched nanowhisker layer interpenetrated with both hydrogels and tissues, creating an interface of high stiffness and strength that kinks and arrests interfacial cracks, ensuring unprecedented fatigue resistance. Further, the nanowhisker glue allows for versatile functionalization at the interface such as photothermal and sonodynamic effects. This work expands the performance and functionality of bioadhesives, opening new possibilities for medical and engineering applications.

Bioadhesives find diverse applications, including wound closure, bleeding control, tissue repair, drug delivery, biomedical implants, and wearable devices[1,2]. Existing bioadhesives mainly consist of polymer chains, such as hydrogels composed of flexible polymer networks swollen in water[3]. Despite achieving tough adhesion on biological tissues through strong interfacial bonding and bulk toughening mechanisms[4,5], bioadhesives remain vulnerable to fatigue fracture under prolonged cyclic loading, resulting in a significant loss of adhesion performance. Specifically, the interfacial fatigue threshold of hydrogel bioadhesives, a value below which fatigue fracture does not occur, is on the order of 10 J m^{-2}, nearly two orders of magnitude lower than the adhesion energy (>1000 J m^{-2}) measured under monotonic loading[6]. The fundamental reason is the inability of the bioadhesive interface to arrest crack propagation, and the depletion of toughening mechanisms such as sacrificial bonds under cyclic loading[7], leading to a small amount of energy required to fracture a single layer of polymer chains at the crack tip[8]. The material constraint of bioadhesives concerns various

[1]Department of Mechanical Engineering, McGill University, Montreal, Quebec, Canada. [2]Center in Green Chemistry and Catalysis, Department of Chemistry, McGill University, Montreal, Quebec, Canada. [3]Aquatic and Crop Resource Development Research Centre, National Research Council of Canada, Montreal, Quebec, Canada. [4]Department of Mechanical Engineering, University of Colorado Boulder, Boulder, Colorado, USA. [5]Department of Materials Engineering, McGill University, Montreal, Quebec, Canada. [6]Department of Biomedical Engineering, McGill University, Montreal, Quebec, Canada. [7]These authors contributed equally: Shuaibing Jiang, Tony Jin. ✉e-mail: audrey.moores@mcgill.ca; jianyu.li@mcgill.ca

applications associated with constantly deforming biological tissues, such as heart and actuating devices like soft robotics[9].

Addressing the challenge of fatigue fracture is the natural evolution of sophisticated nano-scaled structures observed in fatigue-resistant biological materials such as bone and plant stems[10]. For instance, the strong adhesion of cartilages/tendons/ligaments to bones arises from a nanostructured interface composed of ordered hydroxyapatite nanocrystals and collagen nanofibrils, enabling mechanical integrity over a million cycles of loading per year[11]. This tough fatigue-resistant bioadhesion could be attributed to the high stiffness and strength of the nanocrystal interface, which binds strongly with adherents. Such interfaces could deconcentrate stress to inhibit cracking and, further, under large loading, kink the crack into adherents, shielding the interface. The principles underlying fatigue resistance in biological interfaces have inspired the development of engineering materials, as manifested in the nanoparticle-reinforced rubbers with high fatigue resistance[12] and the nanocrystalline interface for fatigue-resistant hydrogel adhesion[13]. Despite these advancements, existing methods such as freeze-thaw and salting-out[13,14] for achieving fatigue-resistant adhesion are clearly incompatible with biological tissues and inapplicable for biomedical applications.

Nanoparticles are promising for the use of bioadhesives in various applications such as hemostasis, wound healing, and bioimaging[15–18]. However, their adhesion energy achieved on biological tissues remains significantly lower than polymer chain counterparts, primarily due to steric hindrance and weak interactions impairing network formation between nanoparticles and tissues (Fig. 1a). Also, the lack of high-resolution characterization of the nanoparticle-tissue interactions at the interface limits mechanistic understanding and material development[19–21]. Overcoming these limitations requires rational design of physical and chemical properties of nanoparticles for strong interactions, integration with tissue-penetrating deployment methods, as well as nanoscale characterization over the tissue-adhesive interface. An emerging class of nanoparticles is nanowhiskers with diameters on the order of nanometers and lengths on the order of hundreds of nanometers. Examples include cellulose and chitin nanocrystals, carbon nanotubes, and chitosan nanowhiskers[22–24]. Among them, chitosan nanowhiskers (ChsNWs) feature a unique combination of geometric, mechanical, and chemical properties. They are rigid nanoparticles in a whisker shape with dimensions of 150–200 nm in length and 5–10 nm in width. The presence of amine and carboxylate groups on their surface allows ChsNWs to form electrostatic interactions and hydrogen bonds between themselves and tissues. Such nanowhiskers of high stiffness and strength, if properly deployed, hold promise to achieve tough fatigue-resistant adhesion on biological tissues.

Here, we report the design, deployment, and mechanism of nanowhisker glues for fatigue-resistant functional bioadhesion. We propose that the nanowhisker glues enable an interface with strong interactions with tissues and hydrogels, and of high stiffness and strength to pin and even kink a crack for fatigue resistance. We demonstrate this principle with ChsNWs. Thanks to their versatile surface chemistry and high aspect ratio, they bind with both the tissue and the hydrogel and form a rigid scaffolding by themselves. As the ChsNWs alone cannot penetrate tissues to form anchorage, we develop three deployment methods, including chemical enhancer, microneedle roller, and ultrasound, to deliver the nanowhiskers across the tissue barriers. When used between the skin and a tough hydrogel matrix, the ChsNWs glue achieves both high adhesion energy (1185 J m^{-2}) and high interfacial fatigue threshold (382 J m^{-2}), outperforming existing bioadhesives, both nanoparticulate and polymeric. To shed light on the adhesion mechanism, we studied the effects of surface chemistry and geometric factors of nanowhiskers on bioadhesion and used a transmission electron microscope (TEM) to visualize the penetration and network formation of ChsNWs at the interface. Furthermore, we functionalized the nanowhisker glues with functional nanoparticles to enable photothermal and sonodynamic effects localized to the interface. This work addresses the fundamental issue limiting bioadhesive performance and would improve and expand the applications of bioadhesives.

Results and discussion

Design strategy

Conventional polymer chains form covalent bonds and/or physical entanglements with biological tissues, resulting in a soft and deformable interface. Chitosan is a notable example of such systems, capable of diffusing into and forming a bridging network between adherends (e.g., tissues and hydrogels), stitching them together akin to a supramolecular suture[25]. One could further reinforce the adhesion by forming covalent bonds between the chitosan and adherends via carbodiimide chemistry[4]. When paired with a tough hydrogel matrix, these polymer-chain glues could achieve high adhesion energy under monotonic loading. However, they cannot resist crack propagation under cyclic loading because a crack only needs to break a polymer chain bridging the interface, resulting in a low interfacial fatigue threshold[6].

To enable fatigue resistance and achieve a high fatigue threshold, we propose the use of rigid, high-aspect-ratio nanoparticles (or nanowhiskers), instead of flexible polymer chains, to form a mechanically stiff and strong interface between hydrogels and tissues (Fig. 1b). These nanowhiskers are expected to bind strongly to the polymer present in the adherents, form a rigid percolated network under physiological environment, and efficiently transmit stress within themselves and with the adhesive matrix. Consequently, when a crack encounters the nanowhisker interface, the rigid nature of the webbed nanowhisker would pin the crack and, further, under large mechanical loading, kink the crack propagation into the tough adhesive matrix. The combination of crack pinning and kinking effects is poised to amplify the interfacial fatigue threshold and resist the crack propagation at the interface under cyclic loading.

To this end, we selected ChsNWs, which combine in a unique way the properties of macromolecular chitosan with a rigid, nano-sized, high-aspect-ratio structure. ChsNWs are accessed via recently developed liquid[26] or solid[27] state synthetic techniques, enabling tunable control of surface amine group density, along with a small amount of carboxylate groups conducive to dispersity under weakly acidic to neutral pH conditions and self-assembly via electrostatic attraction.

Deployment methods

In an initial test, we directly applied a ChsNWs suspension (pH = 5-6) onto porcine skin, prior to pressing an alginate-polyacrylamide hydrogel upon it. The adhesion energy between the two adherends (skin and hydrogel) was low at 18 J m^{-2}, as measured by a modified lap-shear test (Fig. 1c, d). This result echoed previous reports that nanoparticles suffer from tissue barrier effects, yielding relatively weak bioadhesion[15].

As tissue barriers impair bioadhesion with ChsNWs on their own, we sought to address this limitation and explored three deployment methods: chemical enhancer, microneedle, and ultrasound treatment (Fig. 1b). By applying ChsNWs along with laurocapram, a chemical enhancer that is a commonly utilized biocompatible additive in cosmetics[28], we increased the adhesion energy to 74 J m^{-2} (Fig. 1c, d). It is worth nothing that a mixed solvent that allows for the well dispersion of both hydrophilic ChsNWs and hydrophobic laurocapram is essential for the enhancing effect. Laurocapram enhances the fluidity of intercellular lipid bilayers in the stratum corneum[28], opening pathways for the nanowhisker to overcome skin barriers.

The second method we tested was micro-needling to mechanically pierce the tissues and deliver ChsNWs for deep tissue penetration. It was realized with a derma roller (microneedle length = 250 μm),

https://doi.org/10.1038/s41467-025-62019-y

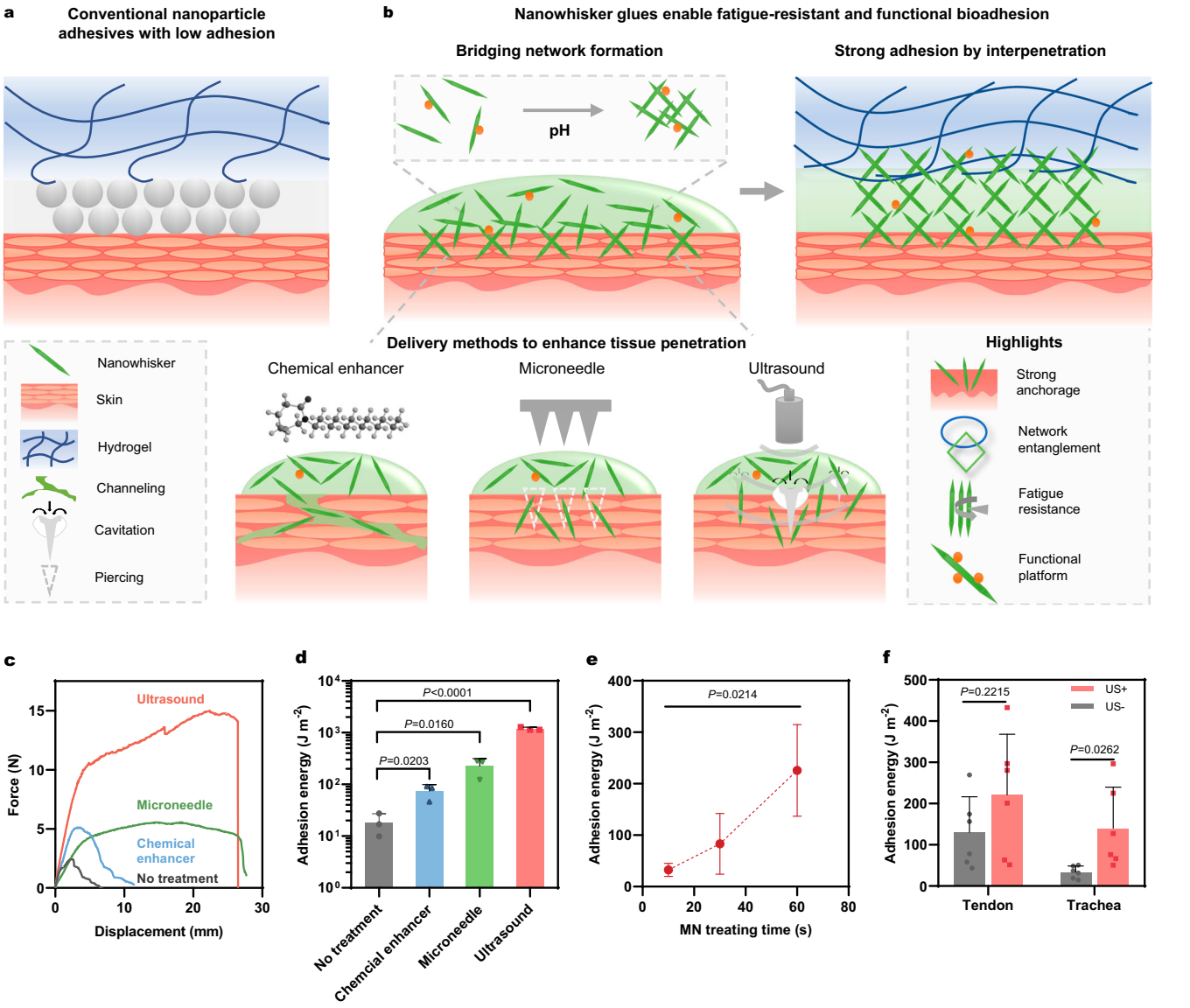

Fig. 1 | Design, deployment, and validation of the nanowhisker glue. **a** Schematic depiction of conventional nanoparticle-based adhesives, which form weak adhesion by physical adsorption. **b** Schematics of nanowhisker glues deployed by chemical enhancer, microneedling, or ultrasound, forming a mechanically rigid and strong interface between the tissue and the hydrogel matrix. Functional nanoparticles conjugated with nanowhiskers are indicated with orange circles. **c**, **d** Force displacement curves and adhesion energy of the ChsNW glue applied between alginate-polyacrylamide hydrogel and porcine skin with different deployment methods. Statistical significance was analyzed using a two-sided Student's *t* test. **e** Correlation between adhesion energy and microneedle (MN) treatment duration. Statistical significance was analyzed using two-sided ANOVA. Data in (**d**, **e**) are presented as mean ± SD ($n = 3$ independent biological replicates). **f** Adhesion energy of ChsNW glue on tendon or trachea with and without ultrasound (US) treatment. Statistical significance was analyzed using a two-sided Student's *t* test. Data are presented as mean ± SD ($n = 6$ independent biological replicates).

applied on the skin area treated with ChsNWs, followed by the placement of the hydrogel matrix. The resulting adhesion energy reached 226 J m^{-2} with just 1 min of microneedling, marking a 13-fold enhancement compared to the non-treatment group (Fig. 1d). This enhancement stems from the mechanical piercing of dense stratum corneum by the microneedles, efficiently delivering ChsNWs into deep tissues (Supplementary Fig. S1). In addition, we observed a positive correlation between adhesion energy and microneedling duration (Fig. 1e), further reinforcing the correlation between tissue penetration and adhesion performance.

We further explored ultrasound treatment as the third deployment method, known to induce cavitation and microjetting, propelling bridging polymers into tissues[29]. We optimized both formulation and ultrasound parameters for the ChsNWs. This optimization yielded a high adhesion energy of 1185 J m^{-2} (Fig. 1d), representing a 66-time enhancement over the non-treatment control, rivaling chitosan chain-based adhesives in performance.

Altogether, these results suggest the importance of tissue penetration in achieving bioadhesion for nanowhisker glues. The properly deployed ChsNWs can form tough adhesion between skin and alginate-polyacrylamide hydrogel. Besides skin, this performance extends to other biological tissues with known tissue barrier effects. The ChsNWs deployed with ultrasound enabled tough adhesion between hydrogels and tendon, as well as trachea (Fig. 1f). Among the three methods tested, the ultrasound afforded the best adhesion performance, so was used in subsequent experiments.

Nanoscale characterization of nanowhisker interface

To reveal how the nanowhisker glues present at the interface and contribute to bioadhesion, we used TEM to characterize the skin-

nanowhisker-hydrogel interface with ultra-high resolution. Given the low contrast of bare ChsNWs in TEM, we functionalized them with gold nanoparticles (Au NPs). The robust and irreversible attachment of Au NPs to ChsNWs was confirmed even after ultrasound treatment (Supplementary Fig. S2). Nanoscale characterization involved microtomography slicing of the hydrogel-on-skin specimens post-fixation with glutaraldehyde and osmium tetroxide as contrast agents (See Supplementary Information for details). In the absence of above-mentioned deployment methods, we observed a distinct separation between the hydrogel and skin layers after sample preparation, with areas devoid of organic matter or Au NPs (Fig. 2a, b). The presence of voids suggests that ChsNWs alone fail to strongly connect and form an extended network bridging the skin and the hydrogel. The adhesion is too weak to even withstand the stress during sample dehydration (Fig. 2b). This finding is further supported by a line-scan analysis using energy dispersive X-ray spectroscopy (EDS), showing the poor penetration of gold, and hence ChsNWs, into the skin without proper deployment methods (Fig. 2c).

In contrast, when ultrasound was applied, an extended ChsNWs network was observed under TEM, penetrating deep into the skin (Fig. 2d, e). The presence of AuNP-ChsNWs at the interface and penetration into the tissue was revealed with high-annular dark field (HAADF) images and EDS mapping (Supplementary Fig. S3). At the interface, the local concentration of Au measured by EDS line-scan was higher than in either the skin or the hydrogel (Fig. 2f). The hydrogel-nanowhisker-skin interface can be seen with three parts. The first part is the hydrogel matrix, showing distinct patterns correlated to the polymer chains of alginate and poly(acrylamide) (Fig. 2g). Possibly due to the steric effect, the ChsNWs did not penetrate deeply into the hydrogel, as indicated by the low Au signal in the EDS line-scan. The second part, interestingly, is the ChsNWs network, where Au NPs are clearly visible in this region, as well as organic matter, presumably ChsNWs themselves. On the hydrogel side, AuNP-ChsNWs are integrated into the hydrogel only at the hydrogel boundary (Fig. 2h). It is clear that the ChsNWs assemble into a densely packed network approximately 2 µm thick, nestled between the hydrogel and the skin (Fig. 2e, i). On the other side, the ChsNWs penetrated deeply into the third region, namely the skin layer, displaying a dark contrast corresponding to the high intensity of AuNP-ChsNWs (Fig. 2j).

Our results present the direct observation of the hydrogel-nanoparticle-skin interface using TEM. This finding is further complemented by H&E staining (Supplementary Fig. S4) and fluorescence imaging (Supplementary Fig. S5). Based on our observations of nanowhiskers, we propose the following mechanism: the nanowhiskers penetrate the tissue, attract the hydrogel, and form an extended network as a cohesive new phase in between (Fig. 2k). This mechanism is embodied with the ChsNWs, carrying both amine and carboxylate groups. They can undergo intercalation through the skin barrier via ultrasound, electrostatically attract the hydrogel and the skin through amine-carboxylate interactions, and assemble into a closely packed extended network at the interface through their surface chemistries, including hydrogen bonds and electrostatic interactions. This proposed mechanism is an alternative to other mechanisms, such as bridging and Pickering, which have been reported for other nanoparticle systems in the literature. The ChsNWs interface could enable strong adhesion between the hydrogel and the tissue, and influence crack propagation under cyclic fatigue loading, which we tested next.

Adhesion performance under monotonic loading

After confirming the formation of a nanowhisker interface, we next studied how it contributes to the adhesion between the hydrogel and the skin. We applied monotonic loading and measured the adhesion energy obtained on porcine skin with ultrasound. As the penetration level of ChsNWs depends on the ultrasound intensity, we investigated the adhesion performance as a function of ultrasound intensity. As expected, the adhesion energy of nanowhisker glue is correlated positively to the applied ultrasound intensity (Supplementary Fig. S6). In comparison with the chitosan chain counterpart, the nanowhisker glue achieves substantially tougher adhesion at a relatively low ultrasound intensity. Specifically, the nanowhisker glue results in the adhesion energy of 626 J m^{-2} at an ultrasound intensity of 16 W cm^{-2}, compared to ~250 J m^{-2} obtained with chitosan chains. Even lower ultrasound intensity can still afford tough adhesion (e.g., 460 J m^{-2} at 8 W cm^{-2}). This is possibly because the inherent low viscosity of nanowhisker glue is favorable for ultrasound cavitation. Such an advantage could mitigate the heating effect observed with ultrasound applied to viscous solutions for better safety.

As the surface chemistry, concentration, and morphology of nanowhiskers determine how they assemble into a bridging network and attract adherents, we varied those factors to devise a rational design for nanowhisker glue. We synthesized the ChsNWs from the chitin nanowhiskers by a solid-phase method[27], which allowed us to control the deacetylation process and led to a series of ChsNWs with varying amine contents (measured as the degree of deacetylation, DDA) (Fig. 3a). Indeed, the lack of surface amines leads to weak bioadhesion notwithstanding the penetration enhancement. With ultrasound deployed, the measured adhesion energy on porcine skin increased by around 11 times when the DDA increased from 32% to 66% (Fig. 3b). A similar dependence of adhesion energy on amine content was also observed when the nanoparticles were deployed using microneedle delivery (Fig. 3c).

We interpret these results as follows. The amines on ChsNWs exert dual effects. On the one hand, they are key to the electrostatic attraction with the negatively charged polymers within the hydrogel and the tissue. On the other hand, when sandwiched between the pH-neutral hydrogels and tissue, these amines deprotonate and form abundant hydrogen bonds among ChsNWs, thereby yielding an extended network at the interface. To further corroborate the importance of surface amines, we conducted experiments using cellulose nanocrystals with the same morphology as ChsNWs but with different surface functional groups, such as hydroxyls and carboxyls. We found cellulose nanocrystals carrying hydroxyls achieve an adhesion energy of 41 J m^{-2} and those carrying carboxylate groups achieve 15 J m^{-2}. These experiments revealed that cellulose nanocrystals, lacking amines, exhibited significantly lower adhesion by an order of magnitude compared to ChsNWs, underscoring the critical role played by amines in this context.

We next characterized the adhesion energy on porcine skin by varying the concentration of ChsNWs in dispersions applied with ultrasound. The adhesion energy exhibits a highly nonlinear dependence on the ChsNWs concentration (Supplementary Fig. S7). Below 1 w/v%, the adhesion is poor, possibly because the density of ChsNWs infused in the tissue is insufficient to form a strong cohesive interface. The adhesion energy peaks at 1 w/v%, and beyond which the adhesion drops to 500 J m^{-2} at 2 w/v%. At higher concentrations, the adhesion energy is very low. We attribute it to the poor dispersion of concentrated ChsNWs, which impairs its diffusion and tissue penetration, as well as ultrasound cavitation. Notably, the optimal tough bioadhesion was achieved for a concentration of 1 w/v%, which could be attributed to the high aspect ratio of the nanowhisker, and despite the low amount of ChsNWs in use, the hydrogel matrix could absorb the water at the interface, significantly concentrating and condensing the ChsNWs into a closely linked extended network layer, as shown in the TEM images.

The morphology of nanoparticles can also influence their bioadhesion performance. Modifying the geometric parameters of ChsNWs over a wide range is technically challenging. To investigate this effect, we synthesized a series of silica nanorods with high aspect ratios and evaluated their performance as bioadhesives. Silica nanorods were selected as a model system due to their well-characterized sol-gel

https://doi.org/10.1038/s41467-025-62019-y

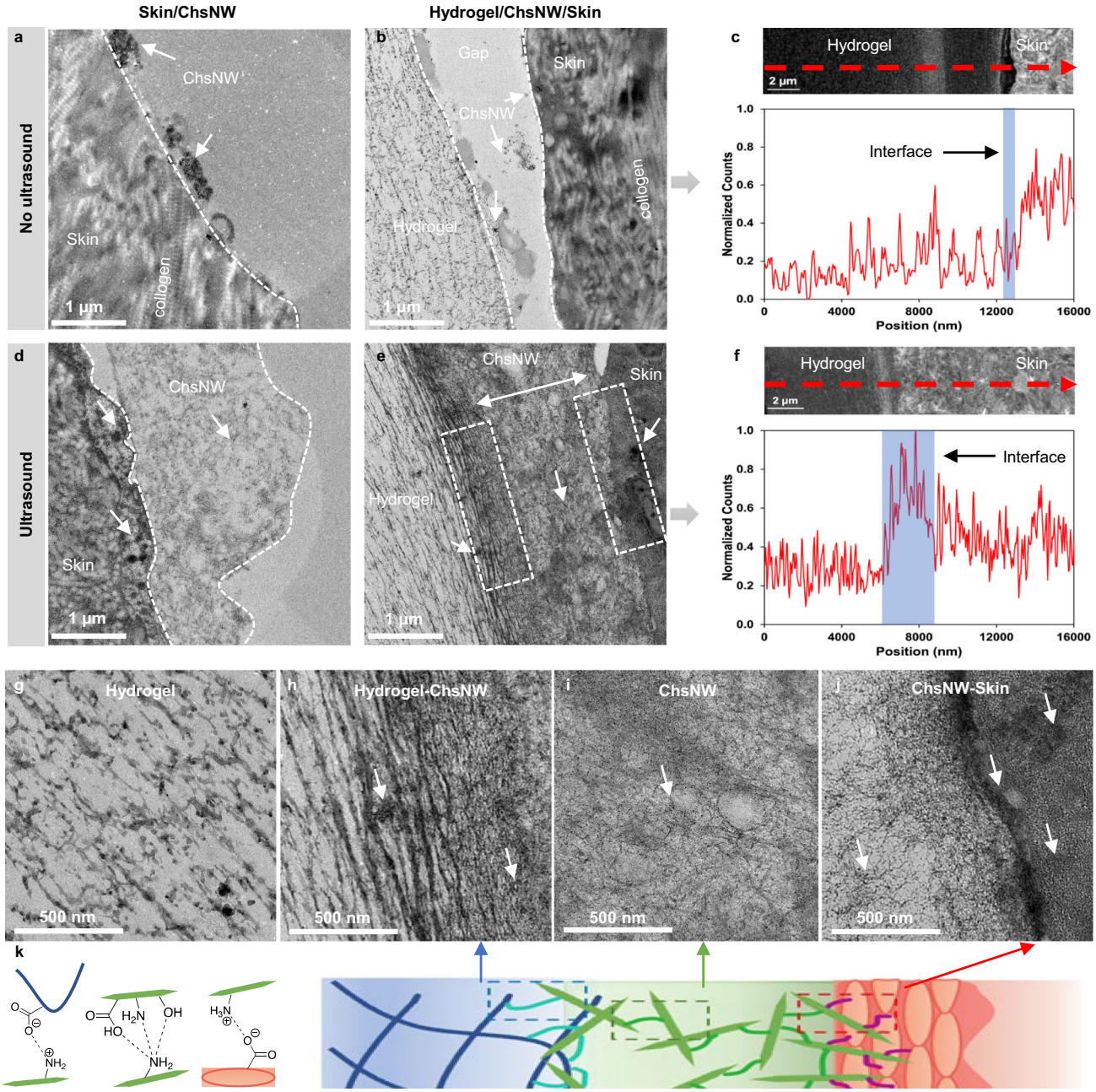

Fig. 2 | Nanoscale characterization of the nanowhisker glue. a, **b** TEM micrographs of microtomography slices of hydrogel on skin using ChsNWs without ultrasound. White dashed lines indicate the boundary between ChsNW and skin or hydrogel, while ChsNWs are labeled with white arrows. **c** TEM micrograph of the interface found in (b, no ultrasound) and its associated EDS mapping with counts of Au signal (lower). **d**, **e** TEM micrographs of microtomography slices of hydrogel on skin using ChsNWs with ultrasound, where the boundaries and ChsNWs are labeled with white dashed lines and white arrows, respectively. **f** TEM micrograph of the interface found in (**e**) ultrasound, and its associated EDS mapping with counts of Au signal (lower). **g**–**j** High magnification TEM micrographs: bare hydrogel, hydrogel-ChsNWs network, ChsNWs network, ChsNWs network-skin. Experiments in (**a**–**j**) were independently repeated at least three times with similar results. **k** Schematics of the interactions between ChsNWs (green), hydrogel (blue), and tissue (orange), as well as the three parts of the hydrogel-nanowhisker-skin interface (right).

chemistry and the ease of tuning their aspect ratios. It is important to note that the surface chemistry of silica nanorods differs from that of ChsNWs, which limits direct comparisons. When deploying the silica rods via ultrasound, we observed a slight increase in adhesion energy with the aspect ratio, yet with no statistical significance (Supplementary Fig. S8). Overall, the adhesion energy observed with silica nanorod were much lower than the ones seen with ChsNWs samples, likely because of the absence of network-forming functionalities on their surface. Our finding echoes previous experimental and computational reports that indicated platelet and cylindrical nanoparticles outperform spherical ones in hydrogel adhesion[20,30].

Interfacial fatigue resistance

Confirming the formation of a rigid networked nanowhisker layer sandwiched between the tissue and the hydrogel, we propose that this interface could resist crack propagation under cyclic fatigue loading. To test this point, we performed cyclic loading tests with 180-degree peeling specimens, which were prepared by adhering alginate-PAAm hydrogel to porcine skin using ChsNWs and ultrasound (Fig. 3d). In this test, a pre-existing crack was introduced at the interface, and the peeling force was precisely controlled by an Instron machine, cycling triangularly between 0 N and a designated maximum force for 10,000 cycles. The ratio of the maximum force F_{max} and the specimen width W

https://doi.org/10.1038/s41467-025-62019-y

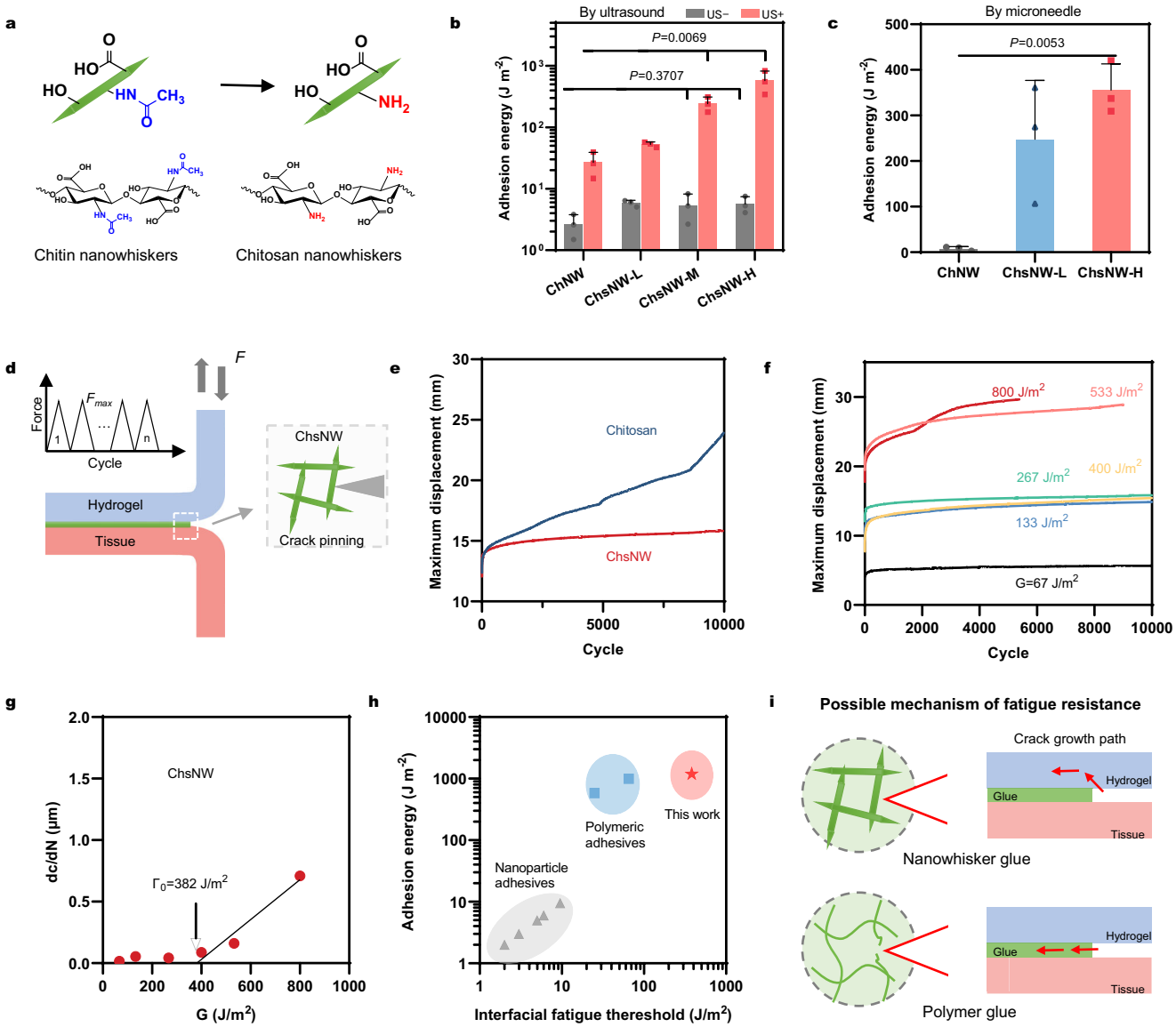

Fig. 3 | Adhesion performance and mechanisms of nanowhisker glues. **a** Controlled deacetylation of chitin nanocrystals leads to ChsNWs with a varied degree of deacetylation and amine content. **b** Adhesion energy as a function of amine content. L, M, and H refer to low (32%), medium (52%), and high (66%) degrees of deacetylation (DDA), respectively. **c** Adhesion energy as a function of amine content for nanoparticles deployed using microneedles. **d** Schematic showing the cyclic peeling test to measure interfacial fatigue threshold and depicting the "crack-pinning" behavior of ChsNWs. The inset is the loading profile. **e** Representative curves of the crack growth as a function of the number of cycles for ChsNWs and chitosan adhesives under $G = 267\ J\ m^{-2}$. **f** The crack growth as a function of the number of cycles at several values of G for nanowhisker glues. **g** Crack growth rate (*dc/dN*) versus applied energy release rate G. The last three data points were linearly extrapolated to obtain the fatigue threshold (i.e., the intercept of the *x*-axis). **h** Ashby plot showing adhesion energy and fatigue threshold relationships for previous nanoparticle adhesives[15,30] polymeric adhesives[6,29], and this work. The interfacial fatigue threshold of nanoparticle adhesives is approximated by their adhesion energies due to the lack of data reported. **i** Mechanisms of fatigue fracture of nanowhisker glue and polymer glue at the interface between hydrogel and tissue. Red arrows indicate the crack path. Data in (**b**, **c**) are presented as mean ± SD ($n = 3$ independent biological replicates). Statistical significance and *P*-values in (**b**, **c**) were determined by two-sided ANOVA.

defines the corresponding energy release rate $G = 2F_{max}/W$. As inextensible backing films were glued to the back of the hydrogel and the tissue, any increase in the maximum peel displacement corresponded to crack propagation, except during the initial period of low cycle numbers when the crack initially blunted without extension. When an energy release rate G of 267 J m^{-2} was applied, we found that the use of ChsNWs pinned the crack at the interface, in contrast to the continuous crack propagation when the chitosan chain was used (Fig. 3e).

Since crack extension depends on the applied loading, we varied the energy release rate. Figure 3f shows negligible crack extension when the energy release rate was below 400 J m^{-2}, beyond which the crack propagates slowly under cyclic loading. To further examine how the crack grows, we calculated the crack growth rate (*dc/dN*) from the displacement-cycle data at plateau regions of large cycle numbers and plotted it as a function of *G*. A clear transition in the crack growth behavior is shown in Fig. 3g. The critical value G for the transition, referred to as the interfacial fatigue threshold, was measured at 382 J m^{-2} through linearly extrapolation and horizontal axis intercept. The interfacial fatigue threshold obtained with ChsNWs was phenomenal when compared with those obtained using its polymer chain counterpart, chitosan, with and without forming additional covalent bonds at the interface (Supplementary Fig. S9)[6,29]. Notably, this value even exceeds that of the fatigue threshold 53 J m^{-2} of the bulk hydrogel in use[31]. We ascribe this difference to the different geometries of the

testing specimen (more discussion can be found in the Supplementary Text).

We summarized and plotted the adhesion energy and interfacial fatigue threshed measured for ChsNWs in this work, alongside data for other nanoparticle-based adhesives and chitosan chain-based adhesives reported in the literature (Fig. 3h). It is important to note that these data encompass different material systems and testing methods so that caution is essential when interpreting this plot. Nevertheless, the plot suggests that the ChsNWs glue deployed with ultrasound achieves a unique combination of high adhesion energy and interfacial fatigue threshold. We attribute the difference between nanowhisker- and polymer chain-based bioadhesion to the high stiffness and strength of the ChsNWs interfacial layer (See the Supplementary Text).

Figure 3i compares the two fatigue fracture mechanisms when a pre-crack grows at the interface between the tissue and the hydrogel matrix. The stiff and rigid ChsNWs layer can pin the pre-crack, and drive crack initiation and propagation into the hydrogel matrix to shield the interface[32] (Fig. 3i **top**). Specifically, as the strength of the nanowhisker film (estimated ~100 MPa) well exceeds that of the hydrogel matrix (~10 kPa), crack initiation occurs preferentially within the hydrogel matrix. Once initiated, the crack propagates inside the hydrogel matrix rather than at the nanowhisker-hydrogel interface due to the significant stiffness contrast, creating a mixed-mode fracture condition. Post-mortem analysis of fatigue specimens confirms this mechanism, with hydrogel residues observed on the skin surface (See the discussion in the Supplementary Text). The experimentally measured fatigue threshold, which correlates to the cohesive fracture of the tough gel matrix, was further enhanced by geometry. On the contrary, the conventional strategies often utilize soft deformable interfaces, composed of flexible polymer chains such as chitosan and polyacrylic acid[4,25]. These interfaces cannot direct the crack propagation and also consume a relatively small amount of energy to fracture a layer of polymer chains at the crack tip, resulting in fatigue vulnerability (Fig. 3i **bottom**).

Localized interfacial functionalization

As the nanowhiskers provide abundant surface sites for functionalization, we explored their use as a platform to localize new and programmable functionalities at the interface. The abundant functional groups on ChsNWs allowed us to bind and deliver other functional materials such as small and large molecules and nanoparticles. Given the size contrast and the extrinsic tissue penetration mechanism, the functional nanowhisker glues allow us to precisely localize the treatment at the interface between the tissue and the adhesive. This would offer significant benefit for various applications, such as photothermal therapies and drug delivery that require localization and avoid large area exposure that causes side effects.

As a proof of concept, we first endowed ChsNWs with photothermal abilities by functionalizing them with gold nanoparticles (AuNP) that are widely used for treating cancer and infection[33]. The same AuNP-ChsNWs was used in the TEM imaging study as described above. We confirmed the functionalized nanowhisker glue can still achieve tough bioadhesion, although there is an expected decrease of adhesion energy due to the surface coverage of bare AuNPs (Supplementary Fig. S10). This issue could be further addressed by modifying Au NPs with the same surface chemistry. In the current work, 2% AuNP-ChsNWs was used to allow for both robust bioadhesion and effective photothermal properties. By utilizing the localized surface plasmon resonance of the Au NPs[34], localized heating is achieved through irradiation of the interface of hydrogel-skin, which we demonstrated was loaded with AuNP-ChsNWs. In this case, a 532 nm green laser was used as it overlaps with the resonance band of AuNP-ChsNWs (Supplementary Fig. S11). We used an IR camera to monitor the temperature at the point of contact between the laser and the interface (Fig. 4a), as well as the back of the specimen to see the localization effect. Within 2 min of laser irradiation, the temperature of the AuNP-ChsNWs interface increased relatively up to 300%, and further raised to 57 °C after 5 min (Fig. 4b, c). In comparison, the pristine ChsNW and blank conditions, without Au NPs, only generated minimal heat through light absorption of the skin. Notably, control experiments confirmed that the temperature increase was localized at the interface of adhesion, and minimal temperature change was seen when measuring the backside of the skin slab during the experiment (Supplementary Fig. S12), suggesting that the heat is unlikely to cause damage to surrounding tissues. We also demonstrate that the temperature of the interface can be controlled in real-time by the ON-OFF cycles of lasers at the minute timescale, which provides precise control for the potential treatments (Fig. 4d). The photothermal nanowhisker glue with localized and controlled heating effect would be suitable for broad applications such as cancer treatment and infection management[35].

In another demonstration, titanium dioxide (TiO_2) nanoparticles were decorated onto ChsNWs to create a reactive oxygen species (ROS)-releasing interface[36,37]. When subjected to a clinical medium-frequency ultrasound (1 MHz), the functionalized TiO_2-ChsNWs could convert water molecules into ROS, such as hydroxyl radicals, singlet oxygen, and hydrogen peroxide (Fig. 4e). We verified this effect using a ROS-responsive fluorescent dye 2′,7′-dichlorofuorescein (DCFH), which clearly increased with ultrasound exposure time (Fig. 4f). In a proof-of-concept in vitro experiment, we adhered a hydrogel loaded with DCFH, a mock prodrug modeling a drug caged by a ROS cleavable functional group, onto porcine muscle tissue with TiO_2-ChsNWs. To show the non-invasive effect of ultrasound, the hydrogel was additionally covered with a 1 cm-thick piece of porcine skin (Fig. 4g). Ultrasound transmission through the skin and hydrogel activated the TiO_2-ChsNWs at the hydrogel-muscle interface. Before ultrasound application, no fluorescence was detected, yet the ROS released from activated TiO_2-ChsNWs triggered strong fluorescence at the interface and detected fluorescence within the hydrogel matrix (Fig. 4h). This design of ROS-releasing nanowhisker glue holds promise for sonodynamic therapy and on-demand drug delivery[36,38]. The functional applications of ROS generated from TiO_2-ChsNWs require further optimization and validation in future studies. The integration of bioadhesion and functionality underscores the potential of functional nanowhisker glues for localized, reliable, targeted therapies, with implications for biomedical applications such as wound management, drug delivery, tissue repair, and regeneration.

To conclude, we reported a class of functional nanowhisker glues to achieve fatigue-resistant bioadhesion and interfacial functionalization. We developed deployment methods such as ultrasound to overcome tissue barriers, resulting in remarkable adhesion energy and interfacial fatigue threshold. The mechanism behind this superior performance lies in the rigid, network-forming nature of ChsNWs, which effectively disperse stress and prevent interfacial cracking. In addition, the integration of programmable functionalities like photothermal and sonodynamic effects further broadens the use of nanowhisker glues. By addressing the fundamental limitations of nanoparticle bioadhesives, this work paves the way for their widespread application in diverse fields, including wound management, tissue engineering, and wearable electronics. The findings underscore the importance of nanostructured materials inspired by natural systems in overcoming engineering challenges that cannot be addressed by existing polymeric systems, offering promising prospects for future advancements in both medicine and engineering.

Methods

Materials

PG chitin, ammonium persulfate, sodium borohydride, sodium hydroxide, hydrogen tetrachloroaurate, Brij C10, nickel (II) chloride, hydrazine, diethylamine, and tetraethylorthosilicate (TEOS), acrylamide,

https://doi.org/10.1038/s41467-025-62019-y

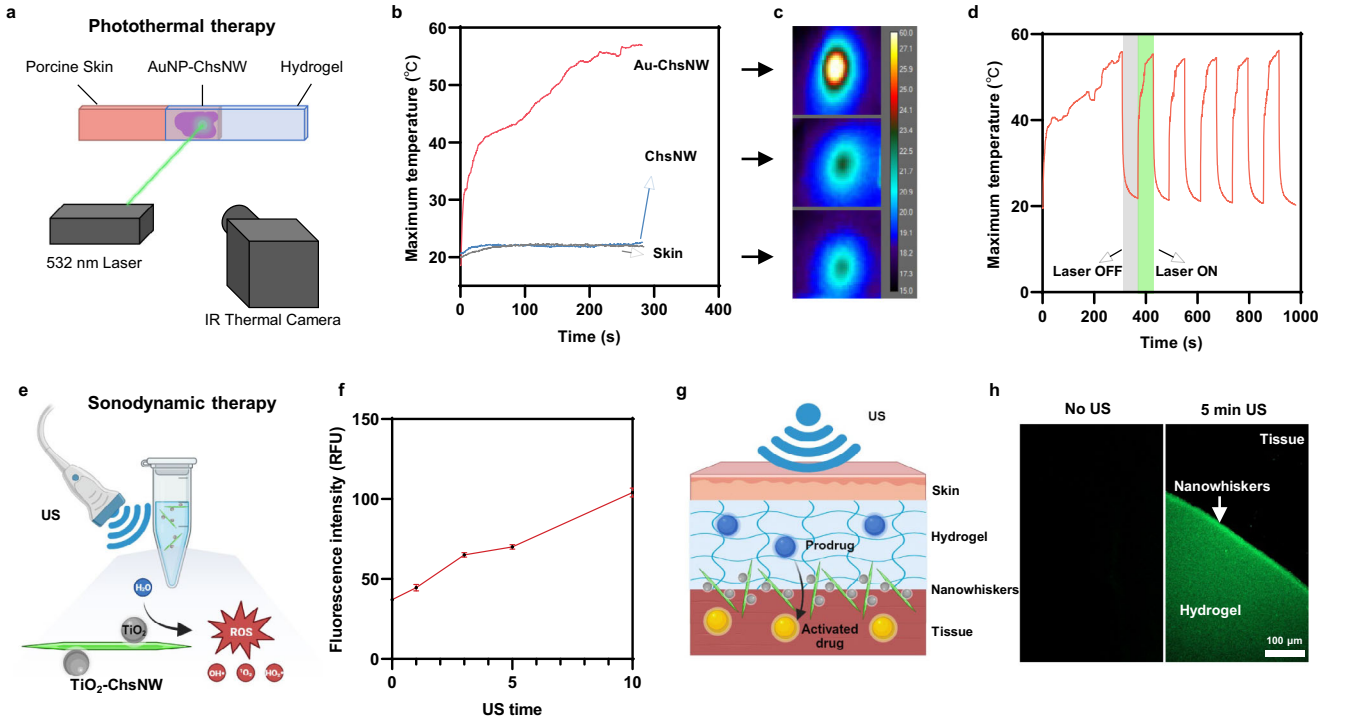

Fig. 4 | Demonstration of functional nanowhisker glues. a Schematic depicting the on-demand photothermal therapy experimental setup. **b** Maximum temperature at the central hotspot of where the laser hits the skin-gel interface using an IR thermal camera. **c** Representative temperature profiles after around 280 s laser irradiation. **d** Recorded maximum temperature of laser-irradiating hotspots. The samples were irradiated for 300 s, then the laser is shut off for 30 s, and turned on for 30 s to reveal the speed of temperature fluctuation. **e** Schematic showing the sonodynamic effect of ChsNWs, which generate reactive oxygen species (ROS) under the field of a clinically used therapeutic ultrasound. **f** Fluorescence intensity of the ROS probe (DCFH) after different times of ultrasound treatment. **g** Schematic showing when the ROS probe encapsulated in a hydrogel as a mock prodrug (representing the drug caged by a ROS cleavable functional group), and then implanted under the skin, the ultrasound can penetrate a depth of skin and activate the prodrug through the sonodynamic effect of ChsNWs. **h** Confocal images before and after ultrasound activation, showing 5 min of ultrasound activates the prodrug reflected by the intense fluorescence at the interface; experiments were independently repeated at least three times with similar results. Data in (**f**)are presented as mean ± SD ($n = 3$). Figures in (**e**, **g**) are created with BioRender.com.

N,N′-methylene bis(acrylamide), tetramethylethylenediamine, calcium sulfate, and 2′,7′-dichlorofluorescin diacetate (DCFH-DA) were all purchased from Sigma Aldrich (St. Louis, MO). High molecular weight sodium alginate (I1G) was acquired from Kimica Corporation. Chitosan (448869) was from Sigma-Aldrich. All commercial chemicals were of reagent grade and used as received.

Synthesis of chitosan nanowhisker

Carboxylated chitin nanowhiskers (ChNWs) and chitosan nanowhiskers (ChsNWs) used in this study were synthesized following a previously described protocol method[26]. In brief, 27.2 g of PG chitin was dispersed in 540 mL of 1 M ammonium persulfate and incubated at 60 °C for 16 h. The resulting mixture was centrifuged at 15,300 × *g* for 10 min, and the pellet was washed six times with deionized water. The purified ChNWs was lyophilized, yielding a white fluffy powder. To produce ChsNWs, 9 g of the ChNWs were combined with 0.9 g of $NaBH_4$ in 900 mL of 40% (w/w) aqueous NaOH and refluxed at 117 °C for 18 h. After reflux, the suspension was centrifuged at 15,300 × *g* for 10 min. The pellet was collected and resuspended in fresh NaOH solution. This centrifugation and resuspension step was repeated two to three times. Following each cycle, a small sample was taken to determine the degree of deacetylation (DDA) via FTIR by monitoring the absorbance at 1030 and 1560 cm^{-1}. When the DDA exceeded 80%, the pellet was suspended in deionized water and centrifuged under the same conditions. Washing was repeated eight times until the supernatant conductivity dropped below 400 μS cm^{-1}. The final pellet was resuspended in water and acidified to pH 5 with 1 M HCl. The resulting ChsNWs were freeze-dried to achieve a white powder (5.7 g, 63% yield) with a final DDA of 88%.

Synthesis of partially deacetylated ChsNWs

The experiments to study the effect of amine density were carried out with ChsNWs prepared using an aging protocol reported by our group before[27]. This protocol allowed for tuning the DDA and produced ChsNWs with low, medium, and high DDA, denoted as ChsNWs-L, ChsNWs-M, and ChsNWs-H, respectively. The synthesis protocol is as follows. To a standard Tupperware glass container was added 1 g of ChNCs and 1 g of NaOH, placed within a 3-dram vial, and a beaker filled with supersaturated potassium sulfate solution to obtain 98% relative humidity. The glass container was then allowed to incubate for 1 day (ChsNWs-L), 3 days (ChsNWs-M), and 6 days (ChsNWs-H). After the allotted incubation period, the as-obtained product was rinsed with methanol to remove excess NaOH until the pH reached neutral. The average yield was 71%. The DDA calculated for the ChsNWs-L, ChsNWs-M, and ChsNWs-H were 32%, 52%, and 66%, respectively.

Synthesis of functionalized ChsNWs

For AuNP-ChsNWs, Au NPs were immobilized onto ChsNWs using a modified literature procedure. First, 250 mg of ChsNWs were suspended in 25 mL of water and mixed with 3.75 mL of $HAuCl_4$ (0.01 M aqueous solution), and magnetically stirred for 10 min in ambient conditions. After, the reaction mixture was placed inside a Teflon liner, and subjected to 4 bar H_2 pressure using a Parr reactor system for 2 h. After, 1 mL of dilute $NaBH_4$ solution (1.5 w/w% aqueous) was added dropwise into the reaction vessel and stirred for 5 min. A purple suspension emerged. The suspension was then lyophilized to yield a fluffy purple powder with 81% yield.

For TiO_2-ChsNWs, 200 mg of ChsNWs was suspended in 200 mL of water. Then, 1 mL of titanium oxysulfate aqueous solution (1.8 M)

was added dropwise to the reaction vessel and stirred at 70 °C for 1 h. The as-obtained TiO_2-labeled ChsNWs suspension was then washed and centrifugated with water 3 times at 15,300 × *g* for 10 min three times.

Synthesis of fluorescent ChsNWs

The fluorescent ChsNWs (FITC-ChsNWs) were prepared by labeling ChsNWs with fluorescein isothiocyanate (FITC) via amine-isothiocyanate reaction. Specifically, 1 g of ChsNWs was dispersed in 100 mL of 0.1 M acetic acid. An equal volume of anhydrous methanol was then added gradually under continuous stirring. FITC (17.5 mg, Sigma) was dissolved in anhydrous methanol (1 mg/mL) and added dropwise to the ChsNW solution. The molar feed ratio of FITC to primary amines on the ChsNWs was set at 2%. The reaction proceeded at room temperature in the dark for 2 h. Following the reaction, the mixture was transferred to 14 kDa MWCO dialysis tubing and dialyzed against deionized water for 3 days. The resulting product was recovered by lyophilization.

Synthesis of silica nanoparticles

The silica nanoparticles in this study was synthesized with a nickel-hydrazine templating protocol. Typically, 4.25 g of Brij C10 was added to 7.5 mL of cyclohexane and heated to 50 °C to dissolve the Brij C10. Then, a variable volume of $NiCl_2$ aqueous solution (0.8 M) was added dropwise to the mixture. For the small, medium, and large silica nanotubes, 0.45 mL, 0.6 mL, and 0.8 mL were added, respectively. After 0.225 mL of hydrazine was added to the mixture, followed by 3 h of stirring at 50 °C. After 0.5 mL of diethylamine and 1 mL of TEOS was added, followed by an additional 3 h stirring. The as-obtained silica nanotubes were then washed with isopropyl alcohol and centrifuged 3 times at 15,300 × *g* for 10 min. The nanotubes were then dispersed in water after the final centrifugation cycle.

Preparation of nanoparticle suspensions

The nanoparticles used in this study include ChsNWs, ChNWs, ChsNWs with a varied degree of deacetylation (ChsNWs-L, ChsNWs-M, and ChsNWs-H), cellulose nanocrystals with varied functionalities (CNC-OH, CNC-COOH), silica nanorods with varied aspect ratios, Au-labeled ChsNWs, and TiO_2-labeled ChsNWs. Typically, the 1% (w/v) suspension of ChsNWs was prepared by mixing 10 mg of ChsNWs with 1 mL DI water, vortexed for 1 min, and dispersed in an ultrasonic bath for 5 min for a final pH of 5 before usage. The suspensions of ChNWs, ChsNWs-L, ChsNWs-M, and ChsNWs-H were prepared at 2% (w/v) in pH = 6 MES buffer. Other nanoparticle suspensions were prepared at 1% (w/v) in DI water unless otherwise mentioned. The 1% (w/v) solution of polymeric chitosan was prepared by dissolving 1 g of chitosan powder into 50 mL of DI water with 400 μL of acetic acid added for a final pH of around 5.

Synthesis of hydrogel matrix

An alginate-polyacrylamide hydrogel was synthesized using a modified protocol previously reported[4]. Briefly, sodium alginate (high molecular weight, I1G, Kimica) and acrylamide (AAm, Sigma-Aldrich) were dissolved in deionized water at concentrations of 2% w/w and 12% w/w, respectively. The solution was stirred overnight until fully clarified. A 20 mL aliquot of this solution was then combined via syringe mixing with 72 μL of 2% w/w N,N′-methylene bis(acrylamide) (MBAA) as a covalent crosslinker, 32 μL of tetramethylethylenediamine (TEMED), 452 μL of ammonium persulfate (APS) at 66 mg/mL, and 250 μL of 15% w/w calcium sulfate ($CaSO_4$) slurry. The final mixture was injected into a sealed glass mold and allowed to polymerize overnight.

Ultrasound-deployed nanowhisker glue

Porcine skin, trachea, and bovine tendon were purchased from a local slaughterhouse, cut into regular strips, stored in the freezer, and thawed at room temperature before use. To confine the nanowhisker suspension on the tissue surface during the ultrasound treatment, a customized plastic ring of 15 mm inner diameter and 15 mm height was first placed on the tissue surface. Then 300 μL of suspension was added into the ring. A US transducer (VWR ultrasonic homogenizer) was subsequently immersed into this suspension and positioned so that the distance between the transducer and tissue surface is 1-2 mm. The typical ultrasound treatment was conducted at 32 W cm^{-2} for 1 min continuously, unless stated otherwise. After ultrasound treatment, a hydrogel patch was placed onto the nanowhisker-covered tissue with the overlapping area of 15 × 15 mm^2 for adhesion and an additional 5 × 15 mm^2 at the end as the non-adherent area (as the initial crack). Compression was applied to the tissue-nanowhisker-hydrogel specimens to enable optimal adhesion, typically for 1 h unless specified otherwise. During the waiting time, the specimens were sealed in humid plastic bags to prevent specimen dehydration. The condition without ultrasound treatment was prepared by directly adding the nanowhisker suspension to the tissue surface for 1 min, followed by the placement of a hydrogel patch without any treatment.

Chemical enhancer-deployed nanowhisker glue

The 1% (w/v) suspension of ChsNWs was prepared by mixing 10 mg of ChsNWs with 1 mL mixed solvent (DI water/isopropanol = 1/1 by volume), followed by vortex and ultrasonication to achieve a well-dispersed suspension. Laurocapram (as known as Azone®) was added to the mixture at 3% (v/v) as the chemical penetration enhancer and vortexed for complete mixing. 300 μL ChsNWs suspension was added onto the skin and left on the surface for 1 min. Then, a hydrogel patch was placed onto the nanowhisker-covered skin as mentioned above for adhesion. The control group is the same as described above.

Microneedle-deployed nanowhisker glue

The 1% (w/v) suspension of ChsNWs dissolved in DI water was used. First, 150 μL ChsNWs suspension was added onto the skin, then a microneedle roller with titanium needles of 250 μm in length was rolling on the skin with the ChsNWs suspension for a certain period, during which another 150 μL ChsNWs suspension was added. The microneedle treating time was set as 10, 30, and 60 s, respectively. After the treatment, a hydrogel patch was placed onto the nanowhisker-covered skin as mentioned above for adhesion. The control group is the same as described above.

Confocal imaging

The adhesive interface of skin-hydrogel specimens and the penetration profiles of ChsNWs into skin were studied by using confocal imaging and fluorescent ChsNWs. Around 300 μL of FITC-ChsNWs suspension was added to porcine skin, treated with chemical enhancer, microneedle, or ultrasound as described above, and no treatment as the control. The skin-hydrogel adhesive specimens were prepared, embedded in OCT compound, and snap-frozen in liquid nitrogen. Frozen sections of 10 μm in thickness were prepared by a microtome, mounted on slides, and imaged using a confocal microscope (LSM710, Zeiss). The samples for characterizing the penetration of ChsNWs into tissues were prepared using porcine skins. FITC-ChsNWs was added on the skin surface, treated for 1 min using different methods as described above. Skin samples were immediately rinsed by DI water thoroughly to removed excessive and unanchored FITC-ChsNWs. Cross-sections were prepared as described above and imaged using a confocal microscope. The penetration depth was analyzed from confocal images.

Histological staining and imaging

The skin-hydrogel adhesive specimens were fixed using 4% paraformaldehyde (PFA) solution for overnight and then incubated with a gradient sucrose solution. Frozen sections of 10 μm in thickness were prepared by a microtome, stained with hematoxylin and eosin stain

(H&E), and mounted on slides. Skin tissue, hydrogel, and adhesive interface of ChsNWs were observed under optical microscopy.

Interface characterization with TEM

Four samples were chosen to be fixed and subjected to microtomography for TEM imaging of the interface. All of these used the porcine skin and hydrogel strip dimensions as stated above. The samples are as follows: (1) 200 μL of 1 wt.% suspension of AuNP-ChsNWs simply pipetted onto the skin surface and left for 1 min, (2) 200 μL of 1 wt.% suspension of AuNP-ChsNWs pipetted onto the skin surface and ultrasonicated for 1 min, (3) 200 μL of 1 wt.% suspension of AuNP-ChsNWs simply pipetted onto the skin surface and left for 1 min, then a strip of hydrogel is placed on top; excess suspension was wiped off with Kimwipes, and (4) 200 μL of 1 wt.% suspension of AuNP-ChsNWs pipetted onto the skin surface and ultrasonicated for 1 min, then a strip of hydrogel is placed on top.

The samples were cut with a scalpel into approximately 2.5 × 5 mm strips. The samples were then submersed in 2.5 wt.% glutaraldehyde fixative in 0.1 M sodium cacodylate with 4 wt.% sucrose overnight at 4 °C. After the post-fixative procedure consisted of submersing the sample in 1 wt.% aqueous osmium tetroxide and 1.5 wt.% potassium ferrocyanide for 2 h at 4 °C (Note that OsO_4 is highly poisonous and can lead to blindness. Handle with extreme caution in a well-ventilated fume hood, and follow protocols outlined in the SDS). After post-fix, wash the samples with doubly distilled water for three times and start dehydration by submersing the samples for 10 min in increasing ratios of acetone:water until 100% acetone.

Fully dehydrated samples were then infiltrated with Epon in acetone. The process takes several days in which each day, the dehydrated samples are submersed in baths of 1:1, 2:1, 3:1 epon:acetone overnight. Finally, the samples are submerged into pure epon for 4 h and under vacuum for 2 h. Finally, the samples are then put into the oven at 60 °C for polymerization. A photograph of the fixed and polymerized samples is given below (Supplementary Fig. S13). The samples were then cut using a Leica Microsystems cryo-ultramicrotome perpendicular to the surface of the samples, such that the cross-sections can be visualized. The slices were placed on standard Cu-mesh TEM grids and analyzed via TEM.

Samples were analyzed using STEM coupled with the high-angle annular dark field (HAADF) detector in a Talos F200X G2 ThermoFisher microscope. The energy dispersive X-ray spectroscopy (EDS) analyses were performed using a SDD Super-X detector at 200 keV for 5 min. The EDS maps for the Au signal shown in this manuscript are displayed, taken the signal at 2.08 eV, characteristic for the Au Mα peak.

Adhesion energy measurements

Modified lap-shear tests were performed with an Instron machine (Model 5965) to characterize the adhesion energy between the hydrogel and the tissue. A hydrogel–tissue adhesion construct was assembled with a 15 mm overlapping adhesion region and a pre-formed 5 mm interfacial crack. Uniaxial tensile loading was applied to the two free ends using an Instron testing machine, while force and displacement were continuously recorded. We assume the shear strain is completely carried by the gel adhesive due to its much smaller elastic modulus than that of skin, the adhesion energy was calculated via $\Gamma_a = t\int_1^{\gamma_c}\tau d\gamma$, where t is the thickness of the gel, τ is the shear stress, γ is the shear strain, and γ_c is the critical shear strain where the interfacial crack starts propagating.

Interfacial fatigue threshold measurements

The 180-degree peeling tests were conducted under cyclic loading using force-control mode to evaluate the interfacial fatigue threshold of hydrogel adhesion to porcine skin. An Instron testing machine applied cyclic forces with amplitude F_a (set below the monotonic peeling force) for N cycles, while the propagation of the interfacial crack (c) was recorded as a function of cycle number (N). The crack growth rate was determined as dc/dN, and the corresponding energy release rate was calculated using $G = 2F_a/W$, where W is the width of the sample. This procedure was repeated across a range of force amplitudes to generate a plot of dc/dN versus G. By linearly extrapolating this plot to the x-axis, the interfacial fatigue threshold, denoted as Γ_O, was obtained.

Photothermal tests

The 2% (w/v) Au-labeled chitosan nanowhiskers (AuNP-ChsNWs) were pipetted onto the skin surface, treated with ultrasound, and then formed adhesion between the skin and hydrogel as described above. A 532 nm green laser with a power of 100 mW was used for laser irradiation. The skin-nanowhisker-hydrogel specimen was attached to the lab stands, and the distance from the laser was set to be around 5 cm. Immediately, the specimen was irradiated by the laser, and an infrared thermal imaging camera was used to map the temperature of the irradiated region, where the maximum temperature of the region was identified to benchmark the photothermal effect. The specimens with unlabeled ChsNWs and without any ChsNWs were included as the control. To test the responsiveness of the photothermal effect, we conducted cyclic photothermal tests by intermittently irradiating the laser for a 30 s ON period followed by a 30 s OFF period, during which the specimen temperature was continuously measured by the thermal imaging camera. Also, we measured the temperature of the back surface of the specimen to show the localized photothermal effect.

Sonodynamic tests

The sonodynamic effect of TiO_2-labeled chitosan nanowhisker (TiO_2-ChsNWs) was firstly evaluated using a previously reported protocol[37]. The 2′,7′-dichlorofuorescein (DCFH), which was converted from DCFH-DA, was used as a probe for measuring reactive oxygen species (ROS). The stock solution of DCFH was prepared accordingly and kept in the dark and on ice before use. TiO_2-ChsNWs was suspended in the DCFH solution at 1% w/v in a 1.5 mL vial. The vials were placed on the therapeutic ultrasound horn with couplant gel for acoustic impedance matching and treated with ultrasound at 1.5 W cm^{-2} for different times. To prevent the overheating ofthe ultrasound horn, it was cooled with ice after each one minute of function. The total time of ultrasound treatment was recorded. The suspensions were centrifuged, and the fluorescence intensity of the supernatants was detected by fluorescence spectrophotometry (BioTek Synergy HTX multi-mode microplate reader, λ_{ex} = 485/20 nm, λ_{em} = 528/20 nm) to evaluate the ROS content. A proof-of-concept of ultrasound-mediated activation and delivery of drugs was performed. DCFH was used as a mock prodrug representing the drug caged by a ROS-cleavable functional group. It was encapsulated in an alginate hydrogel at a concentration of 10 mg mL^{-1}. The hydrogel was then sandwiched between a piece of porcine skin (1 cm in thickness) and porcine muscle tissue. The ultrasound horn was placed onto the skin and can penetrate the depth of the skin and activate the prodrug through the sonodynamic effect of ChsNWs. After ultrasound treatment, the samples were observed by confocal imaging.

Statistical analysis

A sample size of $N \geq 3$ was used for all experiments. Data are shown as mean ± S.D. Statistical analysis was performed using one-way ANOVA and post hoc Tukey tests for multiple comparisons or Student's t tests for comparison between two groups (Prism 9). P-values < 0.05 were considered statistically significant.

Reporting summary

Further information on research design is available in the Nature Portfolio Reporting Summary linked to this article.

Data availability

All data supporting the findings of this study are available within the Article and its Supplementary Information. All data underlying this study are available from the corresponding author upon request.

References

1. Ma, Z., Bao, G. & Li, J. Multifaceted design and emerging applications of tissue adhesives. *Adv. Mater.* **33**, 2007663 (2021).
2. Nam, S. & Mooney, D. Polymeric tissue adhesives. *Chem. Rev.* **121**, 11336–11384 (2021).
3. Yang, J., Bai, R., Chen, B. & Suo, Z. Hydrogel adhesion: a supramolecular synergy of chemistry, topology, and mechanics. *Adv. Funct. Mater.* **30**, 1901693 (2019).
4. Li, J. et al. Tough adhesives for diverse wet surfaces. *Science* **357**, 378–381 (2017).
5. Yuk, H. et al. Dry double-sided tape for adhesion of wet tissues and devices. *Nature* **575**, 169–174 (2019).
6. Ni, X., Chen, C. & Li, J. Interfacial fatigue fracture of tissue adhesive hydrogels. *Extrem. Mech. Lett.* **34**, 100601 (2019).
7. Bai, R., Yang, J. & Suo, Z. Fatigue of hydrogels. *Eur. J. Mech.* **74**, 337–370 (2019).
8. Zhang, W., Gao, Y., Yang, H., Suo, Z. & Lu, T. Fatigue-resistant adhesion I. Long-chain polymers as elastic dissipaters. *Extrem. Mech. Lett.* **39**, 100813 (2020).
9. Zhao, X. et al. Soft materials by design: unconventional polymer networks give extreme properties. *Chem. Rev.* **121**, 4309–4372 (2021).
10. Nepal, D. et al. Hierarchically structured bioinspired nanocomposites. *Nat. Mater.* **22**, 18–35 (2023).
11. Moretti, M. et al. Structural characterization and reliable biomechanical assessment of integrative cartilage repair. *J. Biomech.* **38**, 1846–1854 (2005).
12. Steck, J., Kim, J., Kutsovsky, Y. & Suo, Z. Multiscale stress deconcentration amplifies fatigue resistance of rubber. *Nature* **624**, 303–308 (2023).
13. Liu, J. et al. Fatigue-resistant adhesion of hydrogels. *Nat. Commun.* **11**, 1071 (2020).
14. Hua, M. et al. Strong tough hydrogels via the synergy of freeze-casting and salting out. *Nature* **590**, 594–599 (2021).
15. Rose, S. et al. Nanoparticle solutions as adhesives for gels and biological tissues. *Nature* **505**, 382–385 (2014).
16. Meddahi-Pelle, A. et al. Organ repair, hemostasis, and in vivo bonding of medical devices by aqueous solutions of nanoparticles. *Angew. Chem. Int. Ed. Engl.* **53**, 6369–6373 (2014).
17. Shin, K. et al. Multifunctional nanoparticles as a tissue adhesive and an injectable marker for image-guided procedures. *Nat. Commun.* **8**, 15807 (2017).
18. Hao, L. T. et al. Strong, multifaceted guanidinium-based adhesion of bioorganic nanoparticles to wet biological tissue. *JACS Au* **1**, 1399–1411 (2021).
19. Cao, Z. & Dobrynin, A. V. Nanoparticles as adhesives for soft polymeric materials. *Macromolecules* **49**, 3586–3592 (2016).
20. Molinari, N. & Angioletti-Uberti, S. Nanoparticle organization controls their potency as universal glues for gels. *Nano Lett.* **18**, 3530–3537 (2018).
21. Pan, Z. et al. Designing nanohesives for rapid, universal, and robust hydrogel adhesion. *Nat. Commun.* **14**, 5378 (2023).
22. Thomas, B. et al. Nanocellulose, a versatile green platform: from biosources to materials and their applications. *Chem. Rev.* **118**, 11575–11625 (2018).
23. Jin, T., Liu, T., Lam, E. & Moores, A. Chitin and chitosan on the nanoscale. *Nanoscale Horiz.* **6**, 505–542 (2021).
24. Baughman, R. H., Zakhidov, A. A. & de Heer, W. A. Carbon nanotubes–the route toward applications. *Science* **297**, 787–792 (2002).
25. Yang, J., Bai, R. & Suo, Z. Topological adhesion of wet materials. *Adv. Mater.* **30**, 1800671 (2018).
26. Jin, T. et al. Carboxylated chitosan nanocrystals: a synthetic route and application as superior support for gold-catalyzed reactions. *Biomacromolecules* **21**, 2236–2245 (2020).
27. Jin, T. et al. Chitosan nanocrystals synthesis via aging and application towards alginate hydrogels for sustainable drug release. *Green. Chem.* **23**, 6527–6537 (2021).
28. López-Cervantes, M. et al. Chemical enhancers for the absorption of substances through the skin: laurocapram and its derivatives. *Drug Dev. Ind. Pharm.* **32**, 267–286 (2006).
29. Ma, Z. et al. Controlled tough bioadhesion mediated by ultrasound. *Science* **377**, 751–755 (2022).
30. Arno, M. C. et al. Exploiting the role of nanoparticle shape in enhancing hydrogel adhesive and mechanical properties. *Nat. Commun.* **11**, 1420 (2020).
31. Bai, R. et al. Fatigue fracture of tough hydrogels. *Extrem. Mech. Lett.* **15**, 91–96 (2017).
32. Suo, Z. & Hutchinson, J. W. Interface crack between two elastic layers. *Int. J. Fract.* **43**, 1–18 (1990).
33. Riley, R. S. & Day, E. S. Gold nanoparticle-mediated photothermal therapy: applications and opportunities for multimodal cancer treatment. *Wiley Interdiscip. Rev. Nanomed. Nanobiotechnol.* **9**, e1449 (2017).
34. Moores, A. & Goettmann, F. D. R. The plasmon band in noble metal nanoparticles: an introduction to theory and applications. *N. J. Chem.* **30**, 1121–1132 (2006).
35. Lim, W. Q. & Gao, Z. Plasmonic nanoparticles in biomedicine. *Nano Today* **11**, 168–188 (2016).
36. Qian, X., Zheng, Y. & Chen, Y. Micro/nanoparticle-augmented sonodynamic therapy (SDT): breaking the depth shallow of photoactivation. *Adv. Mater.* **28**, 8097–8129 (2016).
37. Wang, Z. Q. et al. An ultrasound-induced self-clearance hydrogel for male reversible contraception. *ACS Nano* **16**, 5515–5528 (2022).
38. Huo, S. et al. Mechanochemical bond scission for the activation of drugs. *Nat. Chem.* **13**, 131–139 (2021).

Acknowledgements

This work was supported by the Natural Sciences and Engineering Research Council of Canada (J.L.: RGPIN-2024-04925, A.M.: RGPIN-2018-05806 & Discovery Accelerator Supplement, E.L.: RGPIN-2023-03519 & Discovery Launch Supplement), National Research Council Ocean program (OCN-500-3), the Canada Foundation for Innovation and the National Institutes of Health of the United States (1R01DC021461). J.L. acknowledges support from the Canada Research Chairs Program and the International Excellence Grants of Karlsruhe Institute of Technology. A.M. thanks the Fonds de Recherche du Québec Nature et Technologies (FRQNT) - Center for Green Chemistry and Catalysis, and McGill University for their financial support. S.J. and Z.Y. acknowledge support from the FRQNT Doctoral Award. T.J. was supported by the Lawrence Light Sustainability Fellowship, the Walter Sumner Fellowship, and the NSERC Doctoral Award. The authors thank the Advanced BioImaging Facility, Johanne Ouellette, and David Liu at the Facility for Electron Microscopy Research at McGill University for help in microscope operation and data collection.

Author contributions

J.L., A.M., S.J. and T.J. conceived the idea and designed the study. S.J. and T.J. carried out the experiments. R.L. and Z.Y. did the theoretical analysis of fatigue-resistant adhesion. T.N. helped with the microneedle and histology experiments. Z.M. assisted with the ultrasound experiment. R.H. helped with the photothermal experiment. Y.C., D.K., and E.L. helped with resources and experiments. S.J. and T.J. analyzed and

interpreted the results. J.L., A.M., S.J. and T.J. wrote the manuscript with inputs from all authors.

Competing interests
The authors declare no competing interests.

Additional information
Supplementary information The online version contains supplementary material available at https://doi.org/10.1038/s41467-025-62019-y.

Correspondence and requests for materials should be addressed to Audrey Moores or Jianyu Li.

Peer review information *Nature Communications* thanks Ji Liu and the other anonymous reviewer(s) for their contribution to the peer review of this work. A peer review file is available.